

Banner appropriate to article type will appear here in typeset article

Pressure fluctuations of liquids under short-time acceleration

Chihiro Kurihara¹, Akihito Kiyama^{2,3}, and Yoshiyuki Tagawa^{1,2,†}

¹Department of Mechanical Systems Engineering, Tokyo University of Agriculture and Technology, Nakacho 2-24-16 Koganei, Tokyo 184-8588, Japan.

²Institute of Global Innovation Research, Tokyo University of Agriculture and Technology, Nakacho 2-24-16 Koganei, Tokyo 184-8588, Japan.

³Department of Mechanical Science, Saitama University, Saitama, Japan.

(Received xx; revised xx; accepted xx)

This study experimentally investigates the pressure fluctuations of liquids in a column under short-time acceleration and demonstrates that the Strouhal number $St [= L/(c\Delta t)$, where L , c , and Δt are the liquid column length, speed of sound, and acceleration duration, respectively] provides a measure of the pressure fluctuations both for limiting cases (i.e. $St \ll 1$ or $St = \infty$) and for intermediate St values. Incompressible fluid theory and water hammer theory respectively imply that the magnitude of the averaged pressure fluctuation \bar{P} becomes negligible for $St \ll 1$ (i.e., in the condition where the duration of acceleration Δt is large enough compared to the acoustic timescale) and tends to $\rho c u_0$ (where u_0 is the change in the liquid velocity) for $St \geq O(1)$ (i.e., in the condition where Δt is small enough). For intermediate St values, there is no consensus on the value of \bar{P} . In our experiments, L , c , and Δt are varied so that $0.02 \leq St \leq 2.2$. The results suggest that the incompressible fluid theory holds only up to $St \sim 0.2$ and that St governs the pressure fluctuations under different experimental conditions for higher St values. The data relating to a hydrogel also tend to collapse to a unified trend. The inception of cavitation in the liquid starts at $St \sim 0.2$ for various Δt , indicating that the liquid pressure becomes negative. To understand this mechanism, we employ a one-dimensional wave propagation model with a pressure wavefront of finite thickness that scales with Δt . The model provides a reasonable description of the experimental results as a function of St . The slight discrepancy between the model and experimental results reveals additional contributing factors such as the container motion and the profile of the pressure wavefront.

1. Introduction

Abrupt liquid motion causes pressure fluctuations inside the liquid column, resulting in significant fluid motion. For example, a large deformation of the free surface (i.e. jets) can occur in Pokrovski's experiment, where a liquid-filled container falls under gravity and hits the floor (Antkowiak et al. 2007). The pressure impulse approach under the incompressible fluid assumption explains the jet formation. Nevertheless, Kiyama et al. (2016) found that sufficiently large acceleration causes cavitation accompanied by jet formation with a vibrating

† Email address for correspondence: tagawayo@cc.tuat.ac.jp

interface. This implies that the acoustic pressure waves propagate in the liquid column (Bao et al. 2023), meaning that the jet liquid behaves as a weakly compressible fluid.

To describe the liquid compressibility, scaling analysis (Batchelor 1967, §6.3, p. 168-) provides three important terms related as

$$\left| \frac{1}{\rho c^2} \frac{\partial p}{\partial t} - \frac{1}{2c^2} \frac{Dq^2}{Dt} + \frac{aU}{c^2} \right| \ll \frac{U}{L}, \quad (1.1)$$

where ρ is the liquid density, c is the speed of sound, p is the pressure, q is a quantity having the same dimensions as velocity, a is the typical acceleration, U is the typical velocity of liquid (e.g., the impact velocity in an example of Pokrovski's experiment), and L is the typical length scale of the liquid system. Note that the flow is assumed to be isentropic. When each term on the left-hand side has a much smaller magnitude than the spatial derivatives of the components of liquid velocity U/L , the liquid behaves as if it were incompressible. This consideration gives three dimensionless incompressibility conditions relating to the Mach number Ma , Strouhal number St , and Froude number Fr , defined as

$$\frac{L}{c\Delta t} = St \ll 1, \quad (1.2)$$

$$\frac{U}{c} = Ma \ll 1, \quad (1.3)$$

$$\frac{aL}{c^2} = Fr^{-1} \ll 1, \quad (1.4)$$

where Δt is the duration required for the development of the pressure field. The Strouhal number St is the ratio of the duration of acceleration Δt to the acoustic timescale L/c ; a detailed explanation will be provided in §3.1. Note that the Froude number Fr is generally expressed as the ratio of the inertial force to gravitational force. The physical meaning of Fr in the above equation is the competition between the pressure change due to the body force (acceleration including gravity) $\sim \rho aL$ and the ambient pressure $\sim \rho c^2$. This dimensionless number aL/c^2 is equivalent to Fr^{-1} , and is also the product of the other two dimensionless numbers (i.e. $Fr^{-1} \sim StMa$) when the typical acceleration can be scaled as $a \sim U/\Delta t$.

In a previous example of Pokrovski's experiment with fluid compressibility effects (Kiyama et al. 2016), the typical values were found to be $U \sim O(10^0)$ m/s, $c \sim O(10^3)$ m/s, $L \sim O(10^{-1})$ m, $\Delta t \sim O(10^{-4})$ s, and $a \sim O(10^4)$ m/s². Under such conditions, $Ma \sim O(10^{-3}) \ll 1$, $St \sim O(10^0)$, and $Fr^{-1} \sim O(10^{-3}) \ll 1$. This suggests that the compressibility effect in Pokrovski's experiment might be scaled with the Strouhal number St , rather than with Ma and Fr . However, Kiyama et al. (2016) did not consider the influence of the acceleration duration (i.e. St).

We tested the above hypothesis in a preliminary experiment. Figure 1 shows the time series of the acceleration a measured at the top of a container filled with silicone oil (10 cSt) as it impacts the floor. The red line indicates the data taken from the tube impacting a metal floor, where the duration of acceleration $\Delta t \sim 0.11$ ms (indicated by the red shading). The blue line presents the data for a resin floor ($\Delta t \sim 0.27$ ms, blue shading). The dimensionless parameters are $St \sim 3.1 \times 10^{-1}$, $Ma \sim 8.2 \times 10^{-4} \ll 1$, and $Fr^{-1} \sim 3.6 \times 10^{-5} \ll 1$ (red) and $St \sim 1.2 \times 10^{-1}$, $Ma \sim 2.1 \times 10^{-3} \ll 1$, and $Fr^{-1} \sim 3.6 \times 10^{-5} \ll 1$ (blue). Although both cases exhibit similar peaks and mean accelerations at impact, the magnitude of later acceleration fluctuations is quite different. The case with the larger Strouhal number St (i.e. a smaller Δt) exhibits more significant acceleration fluctuations for $t > \Delta t$. This confirms that the short-term acceleration induces pressure waves in the liquid column, even when $Ma \ll 1$ and $Fr^{-1} \ll 1$. We conjectured that the influence of Δt (and thus St) became visible there,

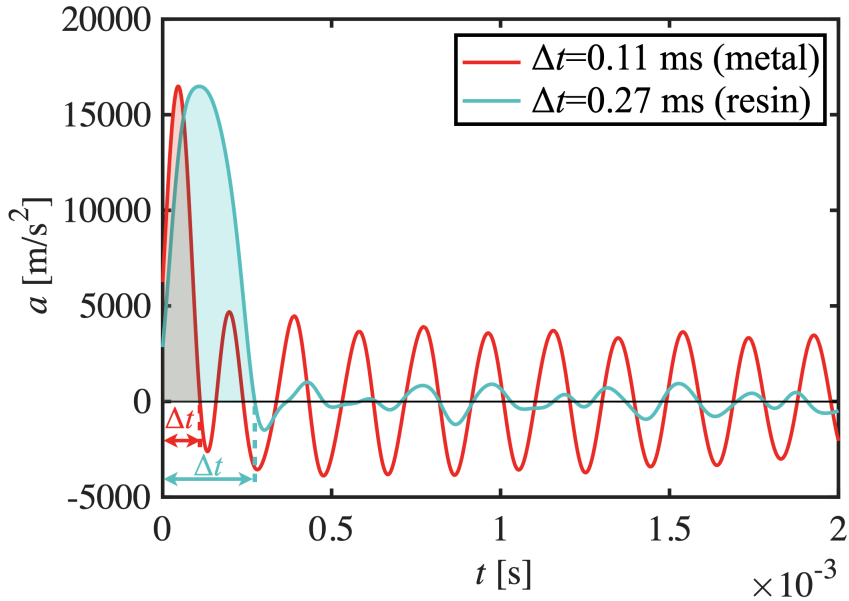


Figure 1: Measured acceleration of a liquid-filled glass container after collision with the floor. Red and blue curves show the acceleration with different floor materials and drop heights. The acceleration during the impact is marked by the shaded area. Although both cases have similar peaks and mean accelerations at impact, the magnitude of the subsequent acceleration fluctuations is quite different.

as the other two dimensionless parameters (Ma, Fr^{-1}) remain much smaller than unity, implying that they are less important. The effects of the acceleration duration Δt are also visible in the fluid motion inside test tubes dropped from the same height (i.e. the same velocity U , see figure 2). The resin floor induces a smooth jet (figure 2a), while the metal floor triggers surface vibrations (figure 2b) and cavitation (figure 2c); see supplementary movies.

To the best of our knowledge, the role of Δt in the development of the pressure field in Pokrovski's experiment has not been systematically investigated. Most existing research took a pressure impulse approach assuming an incompressible flow and a constant Δt which is greater than the acoustic timescale L/c , i.e. $St \ll 1$ (Antkowiak et al. 2007; Pan et al. 2017). In this approach, the pressure field of the liquid is fully developed immediately after the impact, and thus the liquid pressure does not change as a function of time. Another approach takes the water hammer theory into account (Kiyama et al. 2016), and thus assumes an instant increment in pressure, i.e. $\Delta t = 0$ (Ghidaoui et al. 2005; Bergant et al. 2006), where $St = \infty$. This assumption predicts periodic pressure fluctuations \bar{P} with a magnitude of $\rho c U$, but does not capture the role of Δt in the development of the pressure field. Existing research has considered one or other of these approaches, but the intermediate region between $St \ll 1$ and $St = \infty$ has rarely been studied.

This paper focuses on the role of St in the pressure fluctuations, especially in the intermediate St regime. We first define the physical meaning of St in §3.1 as a function of Δt , and examine the experimental data with various liquid depths L , velocities U , acceleration durations Δt , and liquid types. The experimental data collapse onto a single curve, suggesting that St is suitable for describing the pressure fluctuations (§3.2). The conditions for the onset of cavitation are derived in §3.2.2 and the pressure fluctuations in a hydrogel are examined

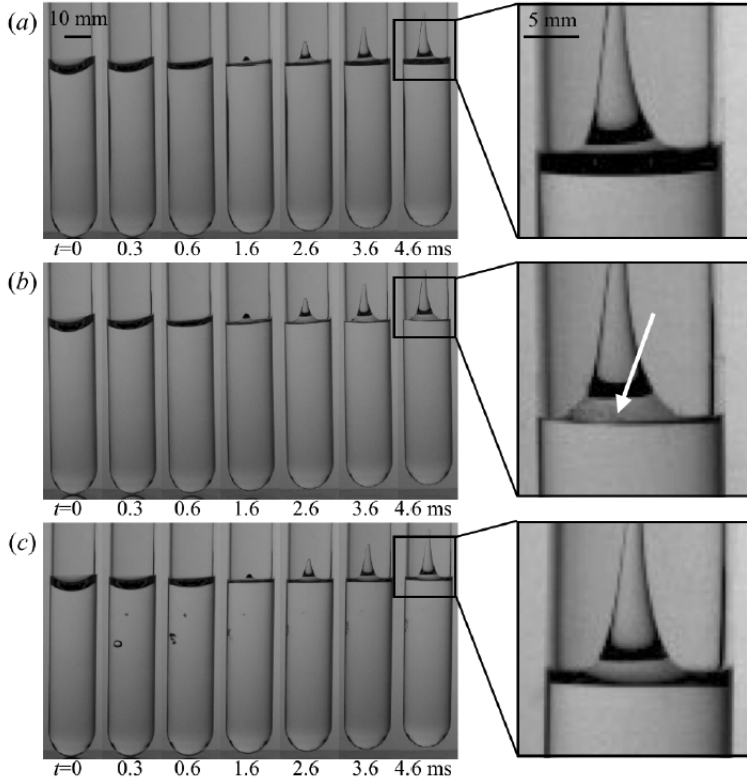


Figure 2: Photographs taken at 100,000 fps using a high-speed camera (Photron SA-X) with a back-light method. The typical velocity is mostly constant (≈ 2.0 m/s) and the height of the jet does not change significantly in each case. The rightmost panels show a magnified view of the free surface at $t=4.6$ ms. (a) Test tube impacting a resin floor, where the free surface remains smooth. (b) Test tube impacting a metal floor, where the free surface vibrates periodically and exhibits a rough texture (marked by a white arrow). (c) Test tube impacting a metal floor, where cavitation occurs inside the liquid. The free surface exhibits a similar response to that in (a). See supplementary movies.

in §3.2.3. In both cases, the present results are shown to be in line with existing pressure results for fluids. We also develop a simple model which takes the effect of the finite thickness of the pressure wavefront into account. This model is used to describe the liquid pressure fluctuations at $t > \Delta t$ based on the one-dimensional wave equation (§3.3). We then compare the output from the proposed model with a wide range of experimental data. The influence of the motion of the surrounding container and the profile of the pressure wavefront is also discussed.

2. Experiments

Figure 3 shows the experimental setup. The container, which is partially filled with a liquid/hydrogel, falls freely and eventually collides with the floor. This accelerates the liquid in the vertical direction opposite to the direction of gravity g . The acceleration of the container is measured with an accelerometer [2350, Showa Sokki Co., sensibility 0.3 pC/(m/s²)] attached to the top of the container. The accelerometer outputs a charge which is

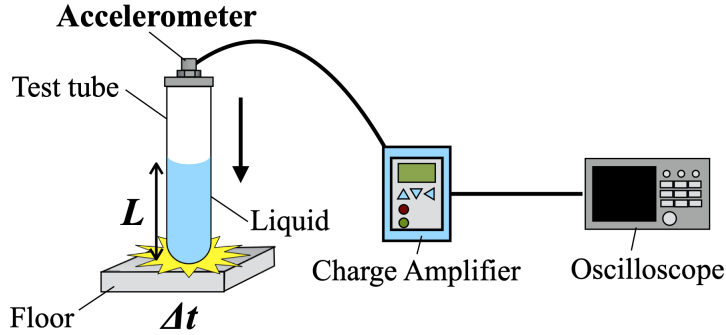


Figure 3: Schematic illustration of the experimental setup. The accelerometer attached to the top of the container records the acceleration a acting on the system. A change in the floor material allows us to change the duration of acceleration Δt . The depth of the liquid in the container L is also varied in our experiments.

converted to a voltage by a charge amplifier (5015A, 5011B, Kistler Co.), and the voltage is recorded by an oscilloscope (Iwatsu Co., ViewGo II, DS 5554-A).

The control parameters are the depth of the liquid column L , the change in the liquid velocity induced by the impact u_0 , the duration of acceleration Δt , and the type of liquid/hydrogel. The depth of the liquid column L ranges from 30–285 mm. We use two borosilicate glass containers of different sizes and masses (see table 1). The characteristic velocity U in this experiment corresponds to the impact velocity u_0 , which is varied from 0.5–3 m/s by adjusting the drop height of the container. The duration of acceleration Δt ranges from 0.1–2.2 ms. To control Δt , different floor materials are used: steel, aluminium, epoxy resin, ABS resin, and rubber. We use different fluids (silicone oils with 1 and 10 cSt obtained from Shin-Etsu Chemical Co., pure water, and ethanol) and a weak gelatin gel (5 wt%) that is expected to flow when it experiences rapid deformation (Kiyama *et al.* 2019) and exhibits similar cavitation to water (Rapet *et al.* 2019). The physical properties of these media are summarized in table 2.

A measured acceleration profile is shown in figure 4(a). A positive value of the acceleration indicates upward vertical acceleration. The grey curve shows the raw acceleration data, whereas the red curve shows the low-pass-filtered data. For filtering, the cut-off frequencies for the 130 and 300 mm tube lengths are 11,000 and 5,000 Hz, respectively; these values are estimated based on the tube length and the speed of sound in glass ($c \sim 5.4 \times 10^3$ m/s). The raw data suddenly change at $t = 0$ when the container impacts the floor, and the acceleration exceeds 1,000 g immediately after the impact. We define Δt as the duration from the collision until the filtered acceleration falls back to 0 m/s^2 . Periodic fluctuations in acceleration are then observed (see figure 4 for $t > t_0$). At $t > t_0$, no fluctuations are visible for an empty container (see inset), indicating that there must be some liquid/hydrogel in the container to observe fluctuations.

The acceleration during Δt for each floor type is shown in figure 4(b). The container is dropped from the same height so that the integral of the acceleration over Δt is similar for all cases. However, a stiffer floor introduces a higher magnitude of acceleration a within a shorter Δt .

The measured acceleration is translated to pressure according to the momentum conservation law: the amplitude of momentum change in the total liquid, Π_L , is equal to that of the

Tube	Length [mm]	Weight [g]	Inner diameter [mm]	Wall thickness [mm]
Short	130	19	14	1
Long	300	66	12	2

Table 1: Specifications of the containers.

Media	Speed of sound c [m/s]	Density ρ_0 [kg/m ³]
Silicone oil (10 cSt)	966.5	935
Silicone oil (1 cSt)	901.3	818
Water	1483	998
Ethanol	1168	789
Gelatin	1391	1052

Table 2: Physical properties of media in a tube. Speed of sound in gelatin is calculated from the acceleration frequency and liquid depth.

container, Π_T . The amplitude of the momentum change in the total liquid is expressed as

$$\Pi_L = \rho A \frac{(\int_0^L u dx)_{max} - (\int_0^L u dx)_{min}}{2} = \rho A L \bar{U}, \quad (2.1)$$

where \bar{U} represents the amplitude of the time difference and the spatial average of the velocity of the liquid, and A indicates the cross-sectional area of the liquid column. The amplitude of the change in momentum of the container is expressed as

$$\Pi_T = mV, \quad (2.2)$$

where m and V are the mass of the container (see table 1) and the amplitude of the velocity fluctuations of the container, respectively. Coupling equations (2.1) and (2.2) gives the following expression:

$$\frac{\bar{U}}{u_0} = \frac{m}{\rho A L} \frac{V}{u_0}. \quad (2.3)$$

We can experimentally determine the right-hand side of equation (2.3). We estimate the velocity of the container V by integrating the acceleration data (see figure 4a). We focus on the velocity after $t = t_0$ and detect the velocity fluctuations v_{max} and v_{min} (see figure 5). Note that v_{max} and v_{min} are taken from the first period after $t = t_0$ to reduce the influence of drift noise. The magnitude of the fluctuations in V is defined as the mean value of v_{max} and v_{min} . Assuming the relationship $\bar{P} = \rho c \bar{U}$, we obtain

$$\frac{\bar{U}}{u_0} = \frac{\bar{P}}{\rho c u_0}. \quad (2.4)$$

Hereafter, the experimental data $\bar{P}/(\rho c u_0)$ are estimated as the representation of $mV/(\rho A L u_0)$.

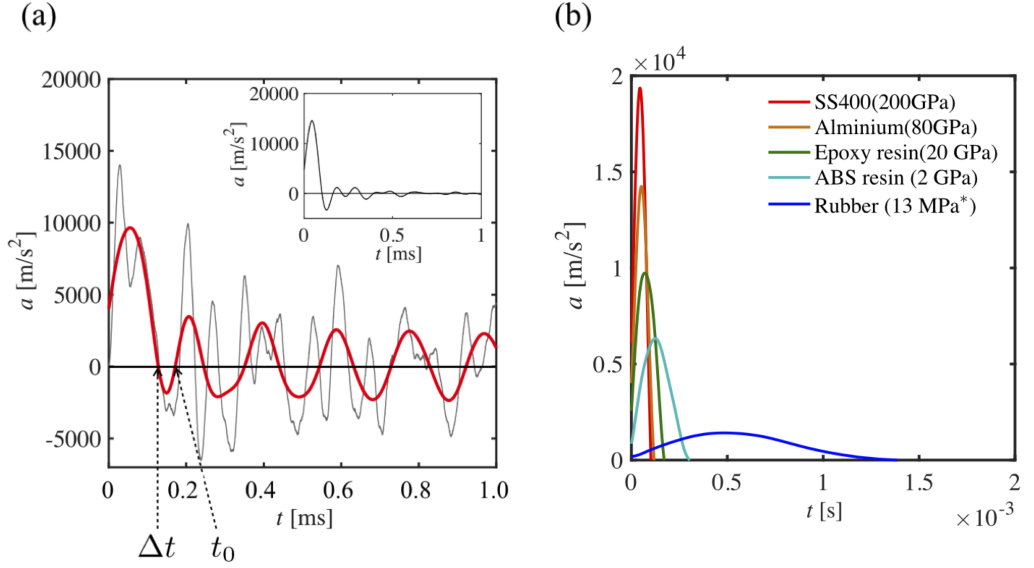


Figure 4: (a) Acceleration of the container partially filled with silicone oil (10 cSt). The grey and red lines represent raw data and data subjected to a low-pass filter. Δt is the duration of acceleration. After t_0 (defined in §3.4), fluctuations in acceleration are visible. The inset shows the acceleration of an empty glass container. (b) Acceleration of each floor type is shown by different colours. Data are obtained from the impact of an empty test tube on each floor material. The Young's modulus is specified in the legend, and * denotes the tensile strength.

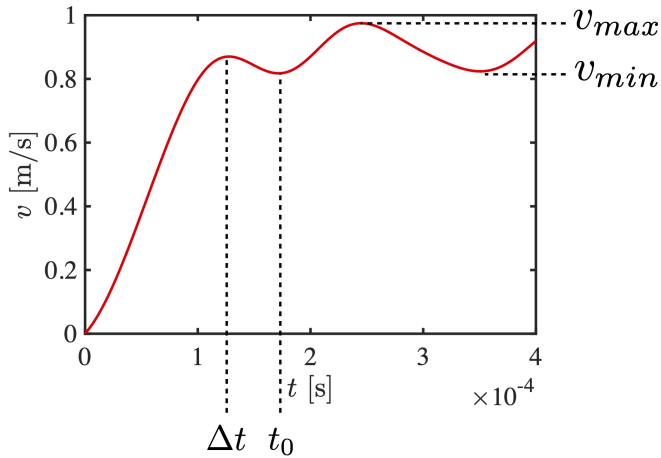


Figure 5: Temporal velocity of the container (i.e. test tube) from the beginning of impact, as calculated by integrating the acceleration data. The peak velocities v_{max} and v_{min} are marked.

3. Results and discussion

3.1. Strouhal number St as an indicator of liquid compressibility

We first derive the Strouhal number St for the one-dimensional system. We assume an infinitesimal disturbance to the velocity, pressure, and density in the inviscid flow. We then

obtain the continuity and Euler equations in terms of the density ρ , velocity u , time t , length x , and pressure p as

$$\frac{\partial \rho}{\partial t} + \rho_0 \frac{\partial u}{\partial x} = 0, \quad (3.1)$$

$$\frac{\partial u}{\partial t} + \frac{1}{\rho_0} \frac{\partial p}{\partial x} = 0. \quad (3.2)$$

Here, ρ_0 is the characteristic liquid density in the far field. The speed of sound in the liquid, c , is defined as $c^2 = \partial p / \partial \rho$. Coupling equations (3.1) and (3.2) yields the wave equation (Leighton 1994) in the form

$$\frac{\partial^2 \Phi}{\partial t^2} - c^2 \frac{\partial^2 \Phi}{\partial x^2} = 0, \quad (3.3)$$

where Φ is the velocity potential (Fujikawa et al. 2005). Introducing dimensionless quantities, the wave equation can be written as

$$St^2 \frac{\partial^2 \Phi^*}{\partial t^{*2}} - \frac{\partial^2 \Phi^*}{\partial x^{*2}} = 0, \quad (3.4)$$

where $St = x/(ut)$ is the Strouhal number. The superscript $*$ denotes dimensionless quantities. In this work, the length of the liquid column L , speed of sound c , and duration of acceleration Δt are substituted for the characteristic length x , speed u , and time t , respectively. The Strouhal number St for our experiments is thus defined as

$$St = \frac{L}{c\Delta t}, \quad (3.5)$$

which is the same form as equation (1.2). In this form, St can be considered as the ratio between the characteristic length of the geometry L and the length scale required to develop the acoustic nature, i.e. the thickness of the wavefront of the pressure wave.

Equation (3.4) also provides a theoretical insight into the fact that St reflects the fluid compressibility, as reported by Reijers et al. (2017). For $St \ll 1$, equation (3.4) can be rewritten as

$$\frac{\partial^2 \Phi^*}{\partial x^{*2}} = 0, \quad (3.6)$$

which describes incompressible and irrotational flow, indicating that the pressure fluctuations due to wave propagation are negligible, as experimentally evidenced in figure 1. In contrast, for $St \ll 1$, the liquid compressibility and pressure fluctuations become visible (figure 1). The pressure fluctuations are derived from the Euler equation (3.2). Integrating this equation with respect to x and assuming $p = p_0$ and $u = 0$ in the far field gives

$$p - p_0 = \rho c U, \quad (3.7)$$

where $\rho c U$ is known as the water hammer pressure; this expression is known as Joukovski's equation (Batchelor 1967; Thompson 1972), a classical formulation for predicting the maximal pressure fluctuations in one-dimensional flows. As explained earlier, in the limit $\Delta t \approx 0$, an instantaneous pressure rise is assumed and the pressure in the liquid jumps from zero to $\rho c U$. According to the above discussion, in our experiments where the characteristic speed is $U = u_0$, the development of pressure \bar{P} is expected to be dominated by the Strouhal number St , which successively connects $\bar{P} = 0$ at $St \ll 1$ and $\bar{P} = \rho c u_0$ at $St \gg 1$.

3.2. Experimental results and remarks

3.2.1. Pressure fluctuations in liquids

Figure 6 compares the amplitude of the spatially averaged liquid pressure change (hereafter, the pressure fluctuation) \bar{P} to the Strouhal number St for different values of Δt and L . The use of different floor materials results in Δt varying from 0.1–2.2 ms, as indicated in the legend. The use of water (Δ), 1 cSt silicone oil (∇), and ethanol (\diamond) allows us to vary the speed of sound c and the liquid density ρ , which are related to the water hammer pressure. In particular, the speed of sound c in water is approximately 1.6 times faster than that in 1 cSt silicone oil. The density ρ of water is approximately 1.3 times higher than that of ethanol.

The experimental data fall onto a single curve that is insensitive to the experimental parameters tested. All of the data for $St > 0.2$ overlap significantly and approach $\bar{P}/(\rho c u_0) \approx 1.0$ when $St \geq O(1)$, whereas the data using resin floors for $St \leq 0.2$ are scattered. The collapse of the data in figure 6 indicates that the Strouhal number St describes the gradual pressure development in a one-dimensional tube. Of the conditions tested, $St \sim 0.2$ is the threshold at which the pressure fluctuations become visible and the transition begins ($\bar{P}/(\rho c u_0) \approx 0.1$).

Figure 6 also contains data for 10 cSt silicone oil (\circ). This has a greater viscosity than the other liquids, but the same trend can be observed because the viscous boundary layer $\delta \sim \sqrt{\nu \Delta t} \sim O(10^{-2})$ mm is expected to be sufficiently thinner than the container radius $\sim O(1)$ mm, as argued in the case of jetting experiments (Onuki et al. 2018; Gordillo et al. 2020). The surface tension does not significantly affect the pressure fluctuations in the present experiments, despite the surface tension of water being approximately 4.3 times higher than that of 1 cSt silicone oil. From the above, the Strouhal number St provides a powerful means of describing the pressure fluctuations inside widely used low-viscosity liquids.

Previous research on similar systems suggests that the accelerating fluid can be modelled as either a compressible fluid (Fogg & Goodson 2009; Kiyama et al. 2016; Daou et al. 2017; Yukisada et al. 2018; Kamamoto et al. 2021a) or an incompressible fluid (Niederhaus & Jacobs 2003; Killian et al. 2012; Daily et al. 2014; Garcia-Atance Fatjo 2016; Pan et al. 2017; Gordillo et al. 2020; Kamamoto et al. 2021b; Krishnan et al. 2022), even if the Strouhal number is in the intermediate region $St \approx O(1)$. Our experimental results (figure 6) obviously show that the pressure wave appears at moderate values of St and its magnitude scales with St : the transition from the “incompressible fluid” region starts at $St \sim O(10^{-1})$ ($St \approx 0.2$ in this experiment) and the “compressible fluid” region is established at $St \sim O(10^1)$. This is reasonably consistent with the case of laser-ablation onto a droplet (Reijers et al. 2017), in which fluid compressibility appears in the flow field (and accordingly the pressure field) at $St \gg 1$.

3.2.2. Cavitation inception following pressure fluctuations

It is thus expected that the Strouhal number St could provide a measure of the tendency for cavitation in a one-dimensional fluid system. The cavitation number for the accelerated liquid (Pan et al. 2017) is written as

$$Ca = \frac{P_{atm} - P_v}{\rho a L}, \quad (3.8)$$

where $a = \bar{U}/\Delta t$. Employing the first-order approximation $\rho L(\bar{U}/\Delta t) \sim St \rho c u_0$, we obtain

$$Ca \sim St^{-1} \frac{P_{atm} - P_v}{\rho c \bar{U}}. \quad (3.9)$$

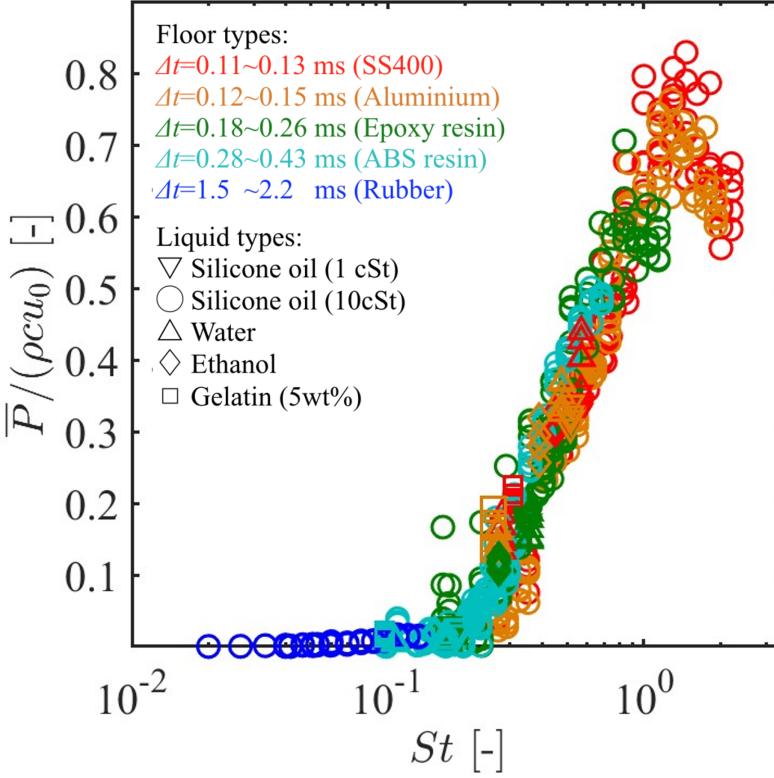


Figure 6: Magnitude of pressure fluctuation $\bar{P}/(\rho c u_0)$ versus Strouhal number St . Data points show experimental results and each plot colour denotes a different floor type. The shapes of the data points correspond to the different liquid types (including a hydrogel), as indicated in the legend.

This expression makes sense for situations in which the influence of Δt is dominant over that of other parameters. If Δt is dominant, Ca and St^{-1} play a similar role and are thus interchangeable. Increasing St decreases Ca , meaning a greater pressure reduction, as expected, and a higher possibility of cavitation occurring (Daily et al. 2014; Pan et al. 2017; Eshraghi et al. 2022). This perhaps explains the findings in previous studies (Garcia-Atance Fatjo 2016; Pan et al. 2017; Xu et al. 2021; Wang et al. 2022), in which the overall cavitation tendency was reasonably classified by only considering Ca as the significance of Δt remained largely unchanged.

Figure 7 shows the probability curves of cavitation in silicone oil (10 cSt) for different floor types. Each marker shows the cavitation probability determined through 10 separate experimental runs. The gradual increase in probability is fitted by the sigmoid function (Maxwell et al. 2013; Hayasaka et al. 2017; Bustamante et al. 2017; Oguri & Ando 2018; Bustamante & Cronin 2019) as

$$Prob. = \frac{1}{2} \left[1 + \operatorname{erf} \left(\frac{St - \alpha}{\beta \sqrt{2}} \right) \right], \quad (3.10)$$

where $\operatorname{erf}()$ is the error function implemented in Matlab, and α and β are the fitting parameters. Overall, cavitation starts at St values as low as 0.2, which agrees well with

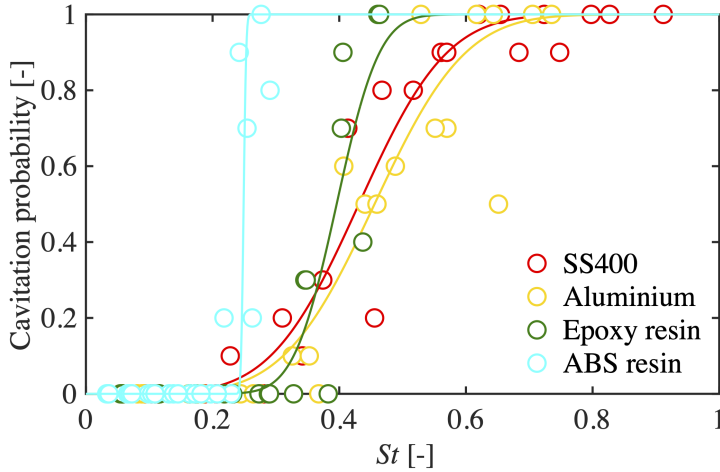


Figure 7: Cavitation probability of silicone oil (10 cSt) for various floor materials, as indicated by colours. The probabilities were experimentally determined through 10 separate experimental runs. The fitting curves were obtained based on equation (3.10), where the fitting parameters are $\alpha = 0.431$ and $\beta = 0.109$ for SS400, $\alpha = 0.456$ and $\beta = 0.113$ for aluminium, $\alpha = 0.396$ and $\beta = 0.053$ for epoxy resin, and $\alpha = 0.249$ and $\beta = 0.0032$ for ABS resin.

the condition for noticeable pressure fluctuations. Closer observation reveals the influence of the floor material. For relatively stiff floors (i.e. SS400 and aluminium), a 50% probability of cavitation is reached at $St = 0.43$ and $St = 0.46$, respectively. For softer floors, the probability curve is steeper (i.e. smaller β values), and the minimum St value required does not vary significantly. The physical reasoning behind this remains unclear, and further investigation is needed. The Δt value varies for softer floors (figure 6), so its influence on the results needs to be clarified.

3.2.3. Pressure fluctuations and cavitation in a hydrogel

The Strouhal number St is still a powerful tool for describing the pressure fluctuations in hydrogels. In figure 6, the gelatin data (squares) for various floor types are in good agreement with the other data for standard fluids. The 5 wt% gelatin gel is a water-based viscoelastic material, which behaves as a soft solid in the rest state. At the moment of impact, it is expected that the gelatin gel could flow due to the fast deformation ($\Delta t \sim O(0.1)$ ms). The above discussion on the Strouhal number St and the water hammer pressure $\rho c u_0$ can be applied to the accelerated hydrogel, although further investigations are needed for a quantitative understanding. Our findings provide an experimental understanding of the inception of cavitation inside the gel (Kang et al. 2017a,b; Kang & Raphael 2018); see the supplementary materials. This phenomenon has been used to address brain injury issues (Yu et al. 2020; Lang et al. 2021).

3.3. Analysis of the pressure fluctuations

We now discuss the basic theoretical framework for predicting the pressure fluctuations. First, we consider a gradual pressure increment at the pressure wavefront to confirm the smooth connection between the “incompressible fluid” region ($St \ll 1$) and the “compressible fluid” region ($St > 1$) as a function of the Strouhal number St (§3.3.1). We then compare the theoretical models and the experimental data (§3.3.2). We discuss the influence of both the container mass and the pressure wavefront profile.

3.3.1. Model considering thickness of pressure wave

This paper focuses on the case of $St = L/(c\Delta t) \approx 1$, where the length of the liquid column L is similar to the length $c\Delta t$. We call $c\Delta t$ the thickness of the pressure wavefront because it corresponds to the length required to establish the water hammer pressure. In such cases, the pressure fluctuations are not determined by the classical formulation assuming an instantaneous pressure rise [equation (3.7)], but are caused by both the temporal pressure change during Δt and the reflection of the pressure wave at the boundaries.

The liquid column in the container has a gas–liquid interface at one end and a solid–liquid interface at the other end. First, we define the function $f^*(\xi^*, t^*)$ describing the liquid pressure change, where ξ^* and t^* are the distance from the solid–liquid interface and the time from the initial impact, respectively. The pressure change propagates in the direction of ξ^* . The wavefront is located at $\xi^* = t^*$ at t^* . We express $f^*(\xi^*, t^*)$ as

$$f^*(\xi^*, t^*) = \begin{cases} 1 & (t^* - 1 \geq \xi^*) \\ I^*(\xi^* - t^* + 1) & (t^* - 1 \leq \xi^* \leq t^*) \\ 0 & (t^* \leq \xi^*), \end{cases} \quad (3.11)$$

where $I^*(\eta)$ is the pressure change in the pressure wavefront, which is modelled as

$$I^*(\eta) = \frac{1}{2} \sin(\eta\pi + \frac{\pi}{2}) + \frac{1}{2}; \quad (3.12)$$

see also figure 8. The reflection of the pressure wave at the boundaries is modelled by assuming the principle of superposition (Thompson 1972). We assume that the mismatching of the acoustic impedance at the gas–liquid and solid–liquid interfaces is significant, and hence we neglect the energy loss upon reflection. The sign of the pressure reverses when the pressure wave reflects at the gas–liquid interface, but does not change when the pressure wave collides the solid–liquid interface. The local pressure in the liquid column p^* is calculated as follows:

$$p^*(\xi^*, t^*, St) = \sum_{i=1}^{\text{ceil}(\frac{t^*}{St})} g^*(\xi^*, t^*, St, i), \quad (3.13)$$

$$g^*(\xi^*, t^*, St, k) = \begin{cases} f^*(kSt - \xi^*, t^*) & (k = 4n) \\ -f^*((k-1)St + \xi^*, t^*) & (k = 4n - 1) \\ -f^*(kSt - \xi^*, t^*) & (k = 4n - 2) \\ f^*((k-1)St + \xi^*, t^*) & (k = 4n - 3), \end{cases}$$

where n is a natural number.

This model allows us to estimate the temporal changes in pressure. We then calculate the amplitude of the spatially averaged pressure in the liquid, \bar{P} . Hereafter, the amplitude of the pressure change $\bar{P}/(\rho cu_0)$ calculated from the above model is compared with that estimated from the experiments, $mV/(\rho ALu_0)$.

3.3.2. Comparison and discussion

We now compare the experimental results (dataset visualised in figure 6) with the model in figure 9(a). The black solid line expresses our model with consideration of the pressure wavefront thickness (see §3.3.1). Figure 9(b) shows a magnified view. For $St = O(10^{-2})$, the fluctuations are not obvious in either the model or the experimental results ($\bar{P}/(\rho cu_0) < 10^{-2}$), suggesting that the liquid behaves as an incompressible fluid. For $St = O(10^{-1})$, the fluctuations in both the experimental results and the model increase notably, which

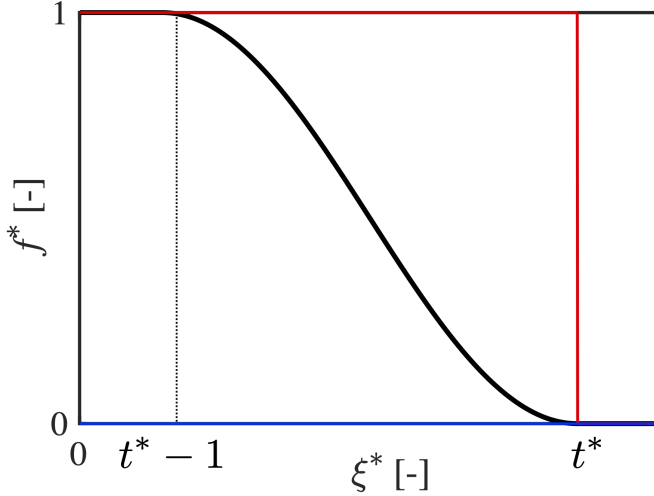


Figure 8: Outline view of the function of pressure change f^* , described by the dimensionless time t^* and dimensionless position ξ^* . Red, blue, and black lines show models with the assumption that the thickness of the wavefront is 0 (i.e. water hammer theory), that the liquid is incompressible, and that the wavefront has a finite thickness, as modelled herein, respectively.

is associated with an increase in the Strouhal number St . Therefore, the effect of liquid compressibility appears at $St = O(10^{-1})$. The proposed model predicts the onset of pressure fluctuations (see figure 9b, $St \sim 0.2$) and captures the overall trend of these fluctuations with respect to St , but overestimates the magnitude of the fluctuations for higher St values ($St < O(10^0)$). Though the model implies that the water hammer pressure $(\bar{P}/(\rho c u_0) = 1.0)$ is reached at higher St values, the experimental results saturate at around $\bar{P}/(\rho c u_0) \sim 0.7$ for $St \sim 1$. Although no data could be obtained for $St > O(10^1)$ due to experimental limitations, we expect that the experimental scenario would differ for higher St values as well because of the influence of the container motion and the profile for the pressure wavefront, as discussed below.

First, we investigate the effects of the container motion. The momentum conservation law for a system consisting of a container and a liquid is

$$mv + A\rho \int_0^L u dx = H(const.), \quad (3.14)$$

where m is the mass of the container, v is the velocity of the container, and A is the cross-sectional area of the liquid column. Note that we neglect the contribution of gravitational acceleration because it is expected to be very small when compared with the acceleration imposed by the impact ($g \ll u_0/\Delta t$). Equation (3.14) can be reformulated as follows in dimensionless quantities:

$$mv^* u_0 + A\rho u_0 c \Delta t \int_0^{St} u^* dx^* = H(const.). \quad (3.15)$$

The momentum conserved in the system, H , is calculated using v^* and u^* immediately after the impact. The velocity of the container v^* is then calculated from the constant momentum H and the instantaneous velocity in the liquid u^* . We incorporate the function f^* in § 3.3.1

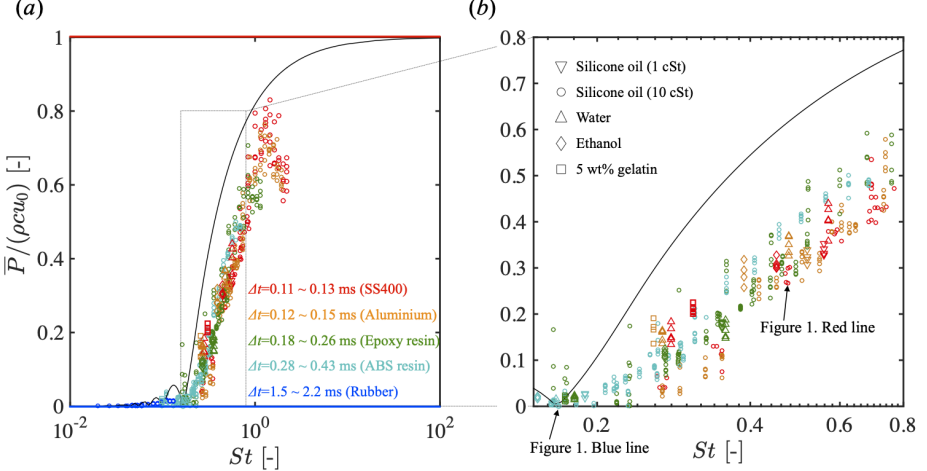


Figure 9: Dimensionless amplitude of the spatial pressure in a liquid as a function of the Strouhal number, St . Data points show experimental results and each plot colour corresponds to a different floor type. The shapes of the data points correspond to different liquids. The red and blue lines show the pressure calculated under the assumptions compressible and incompressible liquids, respectively. The black thin line represents the calculation result using the model (§3.3.1).

into the velocity of the container, v^* , as

$$f^*(\xi^*, t^*) = \begin{cases} v^* & (t^* - 1 \geq \xi^*) \\ I^*(\xi^* - t^* + 1) & (t^* - 1 \leq \xi^* \leq t^*) \\ 0 & (t^* \leq \xi^*). \end{cases} \quad (3.16)$$

The pressure in the liquid is calculated from equation (3.13) using the function f^* . The velocity of the liquid, u^* , is calculated from the following equation:

$$u^*(\xi^*, t^*, St) = \sum_{i=1}^{\text{ceil}(\frac{t^*}{St})} h^*(\xi^*, t^*, St, i), \quad (3.17)$$

$$h^*(\xi^*, t^*, St, k) = \begin{cases} -f^*(kSt - \xi^*, t^*) & (k = 4n) \\ -f^*((k-1)St + \xi^*, t^*) & (k = 4n - 1) \\ f^*(kSt - \xi^*, t^*) & (k = 4n - 2) \\ f^*((k-1)St + \xi^*, t^*) & (k = 4n - 3). \end{cases}$$

The velocity of the container, v^* , is dependent on the momentum of the liquid, which implies some dependence on L , m , A , and ρ [equation (3.15)], and can be interchanged with the pressure, as we did for the experimental data. Considering the velocity change of the container, the amplitude of the pressure fluctuations in the liquid is not only defined by the Strouhal number St and the water hammer pressure.

The revised model is compared with the experimental results in the case of an epoxy resin floor (figure 10). We used two different tubes to vary the mass; the filled and open circles represent the data for the long and short tubes, respectively. The dashed and dotted lines correspond to the model for the long and short tubes, respectively. The revised model taking the change in container velocity into account improves accuracy in terms of the overestimation observed in the original models. The revised model for different tubes also

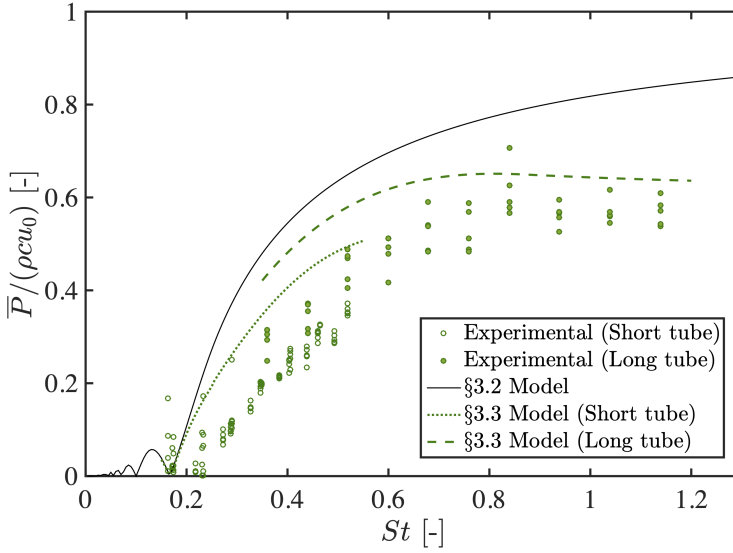


Figure 10: Effect of container motion on the pressure fluctuations in a liquid. Open (filled) circles show experimental results using short (long) tube. The dotted (dashed) line shows the model results considering the motion of the short (long) container.

predicts the influence of the tube types, whereas such variations might be not necessarily visible in the experimental data.

We also tested the effect of the pressure wavefront profile. For comparison purposes, we used a simple profile, illustrated by the dot-dashed line in figure 11(a). This is expressed by $I^*(\eta)$ in equation (3.11), which is defined as

$$I^*(\eta) = 1 - \eta. \quad (3.18)$$

This model overpredicts the pressure fluctuations for smaller St values ($St < O(10^{-1})$), but gives better agreement for larger St values (figure 11b). This suggests that the profile of the pressure wavefront could affect the accuracy of the model predictions, which provides a possible explanation for the difference between the experimental results and the original model (figure 9). In our experiments, the profile of the pressure wavefront is assumed to be dependent on the floor material. Hence, the effect of the pressure profile causes variations in the pressure fluctuations measured experimentally at the same St as well as the cavitation trend for each floor type.

In addition to the above considerations, there are two possible reasons for differences between the model and experiments: the vibration of the container and the curvature of the bottom of the container. Although the model does not consider the effect of vibrations in the container, this phenomenon was indeed observed in the experiments (see figure 4a). The momentum in the experimental system is converted to vibrations. The vibration of the container after the rebound might also be related to the amount of liquid inside the system (Killian et al. 2012; Kiyama et al. 2016; Andrade et al. 2023). Additionally, the model does not consider the curvature of the bottom of the container, which leads to the formation of

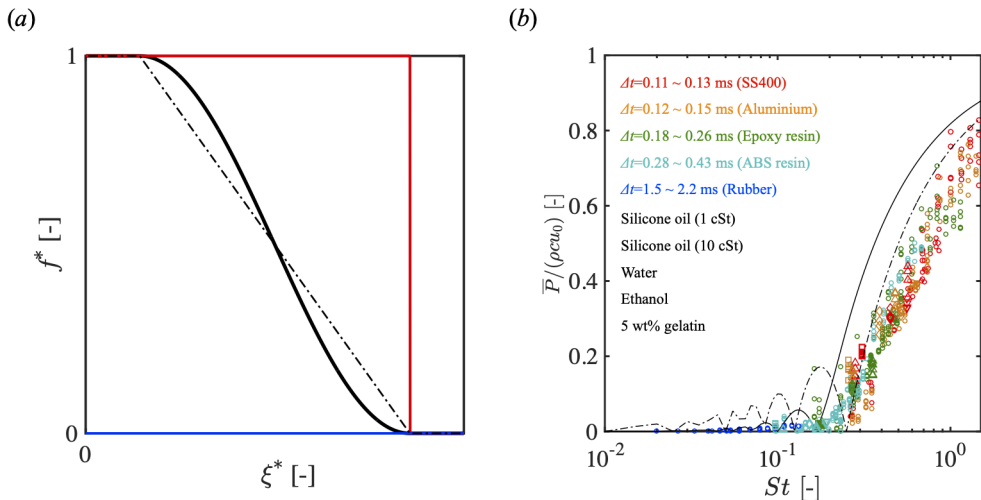


Figure 11: (a) Profile of pressure wavefront. (b) Dimensionless fluctuations in water hammer pressure with respect to Strouhal number. The solid and dot-dashed lines represent different wavefront profiles.

a plane wave in this region. However, we used a container with a rounded bottom in the experiments. A radial phase lag is likely to occur and the fluctuations will differ from those of the model.

4. Conclusions

This paper has shown that the Strouhal number St provides a measure of the fluid compressibility in a one-dimensional system, unlike other dimensionless indicators such as Ma and Fr . Experiments with various liquid column depths inside a tube were performed at different liquid velocities, acceleration durations, and media types (four standard liquids and one hydrogel), producing a wide range of Strouhal numbers, $0.02 \leq St \leq 2.2$. The pressure fluctuations, which were calculated based on the measured acceleration, indicate a unified trend as a function of St for a wide range of parameters (figure 6), suggesting that St gives a good measure of the liquid compressibility in cases where the pressure impulse approach breaks down. Our experimental findings regarding the importance of St are consistent with those from numerical work on bursting droplets (Reijers et al. 2017), suggesting that our discussion related to St might even be applicable in different geometries. We also found that St is useful for describing the cavitation tendency (figure 7). In addition to empirical relations, we derived a conceptual model in which a modified version of water hammer theory accounts for the finite thickness of the pressure wavefront. This simple model describes the overall trend of the experimental data: the magnitude of the pressure fluctuations increases as the Strouhal number St increases (figure 9). Implementing corrections in the model allowed us to show that both the motion of the surrounding container and the profile of the pressure wavefront influence the pressure development (see figures 10 and 11).

Acknowledgements

We thank Prof. J. Rodríguez-Rodríguez for fruitful discussions. We also thank Dr. Andres Franco-Gomez, Prof. Masakazu Muto, Dr. Hajime Onuki, Dr. Prasad Sonar

from Tokyo University of Agriculture and Technology for proofreading the manuscript and making a number of helpful suggestions. This work was partly supported by JSPS KAKENHI through grant numbers JP16J08521, JP17H01246, JP20H00223, JP20H00222, JP20K20972, and JP23K19089, the Japan Science and Technology Agency PRESTO (Grant No. JPMJPR21O5), and Japan Agency for Medical Research and Development (Grant No. JP22he0422016) and by funding from the Institute of Global Innovation Research at the Tokyo University of Agriculture and Technology.

REFERENCES

- ANDRADE, K., CATALÁN, J., MARÍN, J. F., SALINAS, V., CASTILLO, G., GORDILLO, L. & GUTIÉRREZ, P. 2023 Swirling fluid reduces the bounce of partially filled containers. *Phys. Rev. Lett.* **130**, 244001.
- ANTKOWIAK, A., BREMOND, N., LE DIZÈS, S. & VILLERMAUX, E. 2007 Short-term dynamics of a density interface following an impact. *J. Fluid Mech.* **577**, 241–250.
- BAO, H., REUTER, F., ZHANG, H., LU, J. & OHL, C. D. 2023 Impact-driven cavitation bubble dynamics. *Experiments in Fluids* **64** (27).
- BARNEY, C. W., DOUGAN, C. E., MCLEOD, K. R., KAZEMI-MORIDANI, A., ZHENG, Y., YE, Z., TIWARI, S., SACLIGIL, I., RIGGLEMAN, R. A., CAI, S., LEE, J. H., PEYTON, S. R., TEW, G. N. & CROSBY, A. J. 2020 Cavitation in soft matter. *Proc. Natl. Acad. Sci.* **117** (17), 9157–9165.
- BATCHELOR, G. K. 1967 *An Introduction to Fluid Dynamics*. Cambridge University Press.
- BERGANT, A., SIMPSON, A. R. & TIJSSSELING, A. S. 2006 Water hammer with column separation: A historical review. *J. Fluids Struct.* **22** (2), 135–171.
- BUSTAMANTE, M. C. & CRONIN, D. S. 2019 Cavitation threshold evaluation of porcine cerebrospinal fluid using a polymeric split Hopkinson pressure bar-confinement chamber apparatus. *J. Mech. Behav. Biomed. Mater.* **100**, 103400–103409.
- BUSTAMANTE, M. C., SINGH, D. & CRONIN, D. S. 2017 Polymeric opkinson bar-confinement chamber apparatus to evaluate fluid cavitation. *Exp. Mech.* **58**, 55–74.
- DAILY, J., PENDLEBURY, J., LANGLEY, K., HURD, R., THOMSON, S. & TRUSCOTT, T. 2014 Catastrophic cracking courtesy of quiescent cavitation. *Phys. Fluids* **26** (9), 091107.
- DAOU, M. M., IGUALADA, E., DUTILLEUL, H., CITERNE, J.-M., RODRÍGUEZ-RODRÍGUEZ, J., ZALESKI, S. & FUSTER, D. 2017 Investigation of the collapse of bubbles after the impact of a piston on a liquid free surface. *AICHE J.* **63** (6), 2483–2495.
- ESHRAHGI, J., VEILLEUX, J.-C., SHI, G., COLLINS, D., ARDEKANI, A. M. & VLACHOS, P. P. 2022 Assessment of cavitation intensity in accelerating syringes of spring-driven autoinjectors. *Pharmaceutical Research* **39**, 2247–2261.
- FOGG, D. W. & GOODSON, K. E. 2009 Bubble-induced water hammer and cavitation in microchannel flow boiling. *J. Heat Transf.* **131** (12), 121006.
- FUJIKAWA, S., TAKEDA, Y., YANO, Y. & MURAI, Y. 2005 *Foundation of Engineering Fluid Mechanics*. Baifukan (in Japanese).
- GARCIA-ATANCE FATJO, G. 2016 New dimensionless number to predict cavitation in accelerated fluid. *Int. J. Comput. Methods Exp. Meas.* **4** (4), 484–492.
- GHIDAOU, M. S., ZHAO, M., MCINNIS, D. A. & AXWORTHY, D. H. 2005 A review of water hammer theory and practice. *Applied Mechanics Reviews* **58**, 49 – 76.
- GORDILLO, J. M., ONUKI, H. & TAGAWA, Y. 2020 Impulsive generation of jets by flow focusing. *Journal of Fluid Mechanics* **894**, A3.
- HAYASAKA, K., KIYAMA, A. & TAGAWA, Y. 2017 Effects of pressure impulse and peak pressure of a shockwave on microjet velocity in a microchannel. *Microfluid. Nanofluid.* **21** (11), 166.
- KAMAMOTO, K., KIYAMA, A., TAGAWA, Y. & ZHANG, X. 2021a Ouzo column under impact: Formation of emulsion jet and oil-lubricated droplet. *Langmuir* **37** (6), 2056–2064, pMID: 33527827.
- KAMAMOTO, K., ONUKI, H. & TAGAWA, Y. 2021b Drop-on-demand painting of highly viscous liquids. *Flow* **1**, E6.
- KANG, W., ASHFAQ, A., O'SHAUGHNESSY, T. & BAGCHI, A. 2017a Cavitation nucleation in gelatin: Experiment and mechanism. *Acta Biomaterialia* **67**, 295–306.
- KANG, W., CHEN, Y.C., BAGCHI, A. & O'SHAUGHNESSY, T.J. 2017b Characterization and detection of acceleration-induced cavitation in soft materials using a drop-tower-based integrated system. *Rev. Sci. Instrum.* **88** (12), 125113–13.

- KANG, W. & RAPHAEL, M. 2018 Acceleration-induced pressure gradients and cavitation in soft biomaterials. *Sci. Rep.* **8** (1), 1–12.
- KILLIAN, T. W., KLAUS, R. A. & TRUSCOTT, T. T. 2012 Rebound and jet formation of a fluid-filled sphere. *Physics of Fluids* **24** (12), 122106.
- KIYAMA, A., MANSOOR, M. M., SPEIRS, N. B., TAGAWA, Y. & TRUSCOTT, T. T. 2019 Gelatine cavity dynamics of high-speed sphere impact. *J. Fluid Mech.* **880**, 707–722.
- KIYAMA, A., TAGAWA, Y., ANDO, K. & KAMEDA, M. 2016 Effects of water hammer and cavitation on jet formation in a test tube. *J. Fluid Mech.* **787**, 224–236.
- KRISHNAN, S., BHARADWAJ, S. V. & VASAN, V. 2022 Impact of freely falling liquid containers and subsequent jetting. *Experiments in Fluids* **63**, 108.
- LANG, J., NATHAN, R., ZHOU, D., ZHANG, X., LI, B. & WU, Q. 2021 Cavitation causes brain injury. *Phys. Fluids* **33**, 031908.
- LEIGHTON, T.G. 1994 *The Acoustic Bubble*. Academic Press.
- MARSH, J. L. & BENTIL, S. A. 2021 Cerebrospinal fluid cavitation as a mechanism of blast-induced traumatic brain injury: A review of current debates, methods, and findings. *Front. Neurol.* **12**, 626393.
- MAXWELL, A. D., CAIN, C. A., HALL, T. L., FOWLKES, J. B. & XU, Z. 2013 Probability of cavitation for single ultrasound pulses applied to tissues and tissue-mimicking materials. *Ultrasound Med. Biol.* **39** (3), 449–465.
- NIEDERHAUS, C. E. & JACOBS, J. W. 2003 Experimental study of the richtmyer–meshkov instability of incompressible fluids. *Journal of Fluid Mechanics* **485**, 243–277.
- OGURI, R. & ANDO, K. 2018 Cavitation bubble nucleation induced by shock-bubble interaction in a gelatin gel. *Phys. Fluids* **30** (5), 051904.
- ONUKI, H., OI, Y. & TAGAWA, Y. 2018 Microjet generator for highly viscous fluids. *Phys. Rev. Appl.* **9** (1), 014035.
- PAN, Z., KIYAMA, A., TAGAWA, Y., DAILY, J., THOMSON, S., HURD, R. & TRUSCOTT, T. T. 2017 Cavitation onset caused by acceleration. *Proc. Natl. Acad. Sci.* **114** (32), 8470–8474.
- RAPET, J., TAGAWA, Y. & OHL, C. D. 2019 Shear-wave generation from cavitation in soft solids. *Appl. Phys. Lett.* **114** (12), 123702–123705.
- REIJERS, S. A., SNOEIJER, J. H. & GELDERBLOM, H. 2017 Droplet deformation by short laser-induced pressure pulses. *J. Fluid Mech.* **828**, 374–394.
- THOMPSON, P. A. 1972 *Compressible Fluid Dynamics*. McGraw-Hill Inc.
- WANG, Z., LIU, S., LI, B., ZUO, Z. & PAN, Z. 2022 Large cavitation bubbles in the tube with a conical-frustum shaped closed end during a transient process. *Physics of Fluids* **34** (6), 063312.
- XU, P., LIU, S., ZUO, Z. & PAN, Z. 2021 On the criteria of large cavitation bubbles in a tube during a transient process. *Journal of Fluid Mechanics* **913**, R6.
- YU, X., AZOR, A., SHARP, D. J. & GHAJARI, M. 2020 Mechanisms of tensile failure of cerebrospinal fluid in blast traumatic brain injury. *Extrem. Mech. Lett.* **38**, 100739.
- YUKISADA, R., KIYAMA, A., ZHANG, X. & TAGAWA, Y. 2018 Enhancement of focused liquid jets by surface bubbles. *Langmuir* **34** (14), 4234–4240.

Supplementary materials

Cavitation in a hydrogel system

The onset of cavitation and the associated dynamics are of great interest in the community, as they contribute to understanding the brain injuries that may occur following a sudden impact (Barney et al. 2020; Marsh & Bentil 2021). Though a similar system observed the onset of cavitation in a gelatin hydrogel using a high-speed camera (Pan et al. 2017), the present study did not perform any direct visualizations. However, comparing acceleration data as a function of time, some cases exhibit enhanced signals at $O(1)$ ms after the impact (see figure 12). These might be related to the perturbation inside the gelatin column, namely the onset of cavitation. This result supports our claim that the present research has the potential to clarify our understanding of acceleration-induced brain injuries, although the sensitivity of measurements is limited.

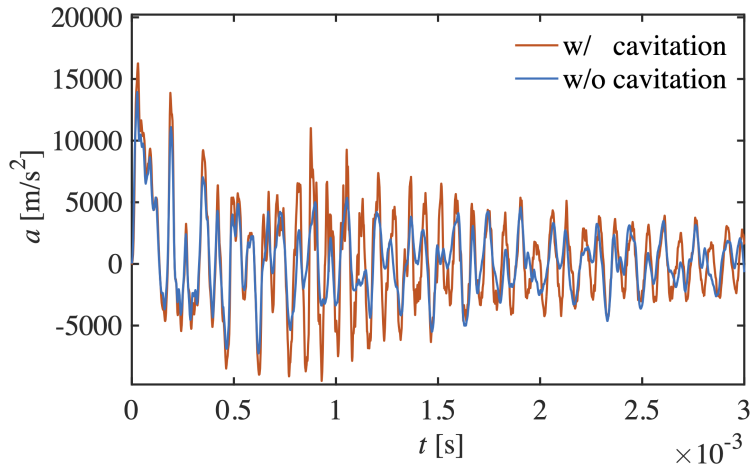


Figure 12: Acceleration a (m/s^2) measured as a function of time t (s). The orange line represents the data with cavitation, while the blue line shows data without cavitation onset. The liquid column height and drop height are $L = 60$ mm and $H = 15$ mm. The Strouhal number St is expected to be greater than 0.2. The signals have not been low-pass filtered to avoid the elimination of high-frequency responses caused by bubble activity.